

See-in-Pairs : Reference Image-Guided Comparative Vision-Language Models for Medical Diagnosis

Ruinan Jin^{1,5}, Gexin Huang^{1,5}, Xinwei Shen², Qiong Zhang³, Yan Shuo Tan⁴, Xiaoxiao Li^{1,5}

¹The University of British Columbia

²ETH Zurich

³Renmin University of China

⁴National University of Singapore

⁵Vector Institute

Abstract

Medical imaging diagnosis presents inherent challenges due to diseases that mimic normal anatomy and exhibit significant inter-patient variability. Clinicians routinely employ comparative reasoning—using reference images from healthy controls or previous patient examinations—to discern subtle yet diagnostically critical abnormalities. However, existing medical vision-language models (VLMs) focus primarily on single-image or single-series analyses and lack explicit mechanisms for comparative reasoning. Conversely, general-purpose VLMs demonstrate strong multi-image comparative reasoning capabilities but lack essential medical-domain knowledge to identify nuanced clinical differences. This work aims to bridge this gap by exploring clinically-inspired comparative analysis within VLMs, leveraging reference images to enhance diagnostic accuracy. Through extensive empirical analysis, we show that providing general-purpose VLMs with query and normative matched reference images, accompanied by clinically-informed comparative prompts, significantly improves diagnostic outcomes compared to single-image baselines, especially after supervised finetuning (SFT). Our contributions highlight the clinical relevance of comparative analysis introduce novel strategies for leveraging reference images in VLMs, empirically demonstrate enhanced performance across multiple medical visual question answering (VQA) tasks, and provide theoretical insights into the efficacy of comparative image analysis in medical diagnosis.

1 Introduction

Medical imaging diagnosis is inherently challenging due to diseases often mimicking normal anatomy or exhibiting high inter-patient variability [1, 2]. These complexities distinguish medical image analysis from general visual recognition tasks, demanding specialized approaches to detect subtle pathological features [3, 4]. One potential approach is to seek inspiration from clinical practice. For example, radiologists routinely leverage reference images—such as scans from healthy controls or a patient’s prior examinations—to identify nuanced abnormalities through pairwise comparisons (Fig. 1). This comparative analysis provides critical diagnostic context, reducing interpretation errors by highlighting disease-relevant deviations.

Neither medical VLMs or general-purpose VLMs are currently capable of medical image comparative analysis. Existing medical VLMs like R2Gen [5], LLaVaMed [6], and XrayGPT [7] focus on single-

image or single-series analysis, lacking explicit mechanisms for cross-image comparative reasoning. Conversely, general-purpose VLMs such as QwenVL-2.5-Instruct [8], NVILA-8b [9], and Phi-3.5-4.12b [10] exhibit strong multi-image reasoning [11] but lack medical-domain priors, limiting their ability to discern clinically meaningful distinctions.

Our work seeks to bridge this gap. Specifically, we investigate the following research question:

Can clinically-inspired comparative reasoning, leveraging reference images, enhance diagnostic accuracy in VLMs for medical imaging tasks?

Prior studies indicate that modifying medical VLMs to develop comparative reasoning capabilities may require extensive additional training samples or substantial architectural modifications [12, 11]. This approach may hence have poor feasibility, given the substantial difficulty associated with curating large-scale medical imaging datasets. On the other hand (see Sec. 4.2), we found that providing general-purpose VLMs with both query and reference images, along with appropriate comparative prompts, significantly improves diagnostic performance compared to single-image queries.

Building on this insight, we propose efficiently adapting general-purpose VLMs’ comparative reasoning capabilities to medical imaging tasks via targeted SFT. Our method moves beyond fine-tuning on individual images by incorporating clinically-inspired negative references, structured as (query, reference, label) training tuples. To further ensure ease of implementation and versatility across various diagnostic scenarios, we leverage readily available or easy-to-obtain healthy control images as *negative* references [13, 14]. These references from healthy samples are chosen to share overlapping, diagnostically irrelevant features with the query image, guiding the model to discern critical pathological differences. Importantly, our comparative strategy distinctly and orthogonally differs from advancing more powerful medical-specific VLMs via pretraining which requires substantial training cost. Rather than competing with these specialized models, our method proposes an efficient and effective approach to enhance general-purpose VLM architectures by introducing explicit clinical comparative diagnosis, thereby addressing inherent limitations of single-image diagnostic approaches in challenging clinical scenarios.

Our contributions include: (1) highlighting the critical challenges and clinical practice motivating the need for comparative diagnosis in medical image analysis; (2) introducing novel approaches leveraging reference images and SFT to improve feature representation learning for query image and diagnosis effectiveness; (3) empirically demonstrating the improved performance of our comparative method compared to baselines in five medical VQA datasets; and (4) providing theoretical understanding of how adopting a comparative method can improve statistical efficiency.

2 Related Work

Advanced Medical Vision-Language Models. Recent medical vision-language models (VLMs) have shown promising applications across various medical imaging modalities, such as radiology [7], pathology [15], and ophthalmology [16]. Models like MedLLaVa [6] and BiomedGPT [17] address a broader spectrum of medical imaging tasks, including visual question answering, diagnostic and report generation. Other specialized models, such as MedViLL [18] and Q2ATransformer [19], have effectively addressed medical VQA through tailored Transformer-based frameworks. Despite their broad applications, most of these models remain limited to single-image analysis. They often overlook how clinicians routinely compare current scans with reference images, such as healthy exemplars. To better support clinical decision-making, medical VLMs should incorporate comparative reasoning strategies that reflect how physicians interpret images in practical contexts.

General VLM with Multi-image Comparison Capability. Recently, general VLMs demonstrate robust capabilities in relation analysis tasks [11]. Specifically, Qwen-VL-2.5-Instruct [8] enables robust image comparison by incorporating co-attention-based multimodal fusion, image-specific positional encoding, and fine-tuning on tasks that require comparative visual reasoning. NVILA-8B [9] enhances visual relational reasoning through a "scale-then-compress" architecture, enabling efficient processing of high-resolution images and long videos, which supports complex image comparisons. Phi-3.5-Vision [10] facilitates advanced image comparison by interleaving visual and textual tokens, allowing the model to perform multi-hop relational analysis across multiple

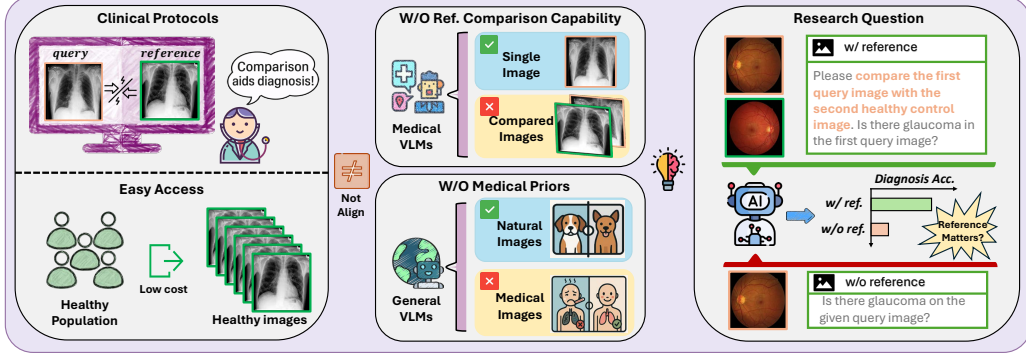


Figure 1: **Illustration of the overall study pipeline.** This work is motivated by clinical practice, where reference images (e.g., healthy control scans) are commonly used for diagnosis. Acquiring such negative reference images is typically cost-efficient given the large healthy population. However, existing medical VLMs are usually trained on single images and rarely consider multi-image settings. While general VLMs possess some image comparison capabilities, they lack medical domain priors. Our study, *Seeing in Pairs* (SiP) investigates the role of incorporating a reference image for disease diagnosis. By jointly training on query and reference image pairs, SiP achieves improved feature representation, more effective sampling (by utilizing readily available healthy control images), and enhanced diagnostic performance.

images. GPT-4V [20] excels in general multimodal understanding, including sophisticated relation analysis tasks. Similarly, LLaVA-v1.5 [21] leverages instruction-tuned data to perform well in visual comparative tasks, whereas Emu2-Chat [22] incorporates extensive multimodal conversational data to facilitate relational visual analysis. However, despite their comparative strengths in relation analysis, these general-purpose VLMs lack critical medical-domain priors necessary for accurately identifying clinically relevant subtle distinctions. Without medical-specific knowledge and contextual understanding, their effectiveness significantly diminishes when applied to medical imaging tasks where nuanced visual distinctions are critical. This absence of domain-specific expertise restricts their practical clinical utility, underscoring the necessity for incorporating explicit medical-domain comparative analysis into vision-language model architectures.

3 See-in-Pairs (SiP) VLMs with Reference images

To address the research question posed in Sec.1, this study focuses exclusively on *closed-ended answer-only* diagnosis using VLMs. For convenience, all notations used in Secs.3 and 5 are summarized in the Appendix. We begin by presenting the problem setup and formalizing inference in the traditional single-image paradigm, then extend the framework to include *matched* healthy-control reference images in Sec 3.1. Next, we introduce our comparative SFT strategy, which enhances comparative analysis by adapting VLMs with comparison capability using well-constructed comparative SFT medical datasets in Sec 3.2.

3.1 SiP Inference

Single Query Image Inference. Let \mathcal{X} be the space of medical images and \mathcal{Q} the space of natural-language prompts. We draw triples (X, Q, A) , where $X \in \mathcal{X}$, $Q \in \mathcal{Q}$, and $A = \{a_1, \dots, a_K\}$ is the potential ground-truth answer list, where a_k could be “yes”, “no”, or disease types. We serialize the (X, Q) pair as the input prompts to the LLM:

$$Z = \langle \text{encoder}(X), \text{encode}(Q) \rangle. \quad (1)$$

Here $\text{encode}(X)$ denotes patch embeddings from a vision encoder. For any candidate answer string, $a_k = \langle t_1, \dots, t_{L_k} \rangle$, where t_i is the i^{th} token and L_k is the maximum length of the given answer. We make a prediction via a VLM parameterized by θ ,

$$\hat{a} = \arg \max_{a_k \in \mathcal{A}} P_{\theta}(a_k | Z), \quad P_{\theta}(a_k | Z) = \prod_{j=1}^{L_k} P_{\theta}(t_j | Z, t_{<j}). \quad (2)$$

for the final prediction.

Inference with Reference Image. To mimic clinical practice, we introduce reference images $X' \in \mathcal{X}'$ with known labels. The labels for X' are set to be negative in diagnosis, such as “no” or “healthy control.”¹ To help the VLM focus on disease-related patterns and reduce the influence of irrelevant factors, such as scanner types or, for some diseases, gender and age, we pair a query image with a negative reference image that shares the same diagnosis-irrelevant features when possible. Unlike single-image inference, we serialize the (X, X', Q) triplet as the input prompts to the LLM:

$$Z' = \langle \text{fusion}(\text{encode}(X), \text{encode}(X')), \text{encode}(Q) \rangle, \quad (3)$$

where fusion is a VLM-dependent fusion operation and then we replace Z with Z' in Eq. 2.

3.2 Improved Performance via Comparative Supervised Fine-tuning (SFT)

While the results of zero-shot testing presented in Sec. 4.2 demonstrate the promise of incorporating reference images into medical imaging diagnosis, we also observe a clear performance gap when relying solely on zero-shot inference using general-purpose VLMs. Following established practices for SFT in generative medical VLMs [6], we focus our updates specifically on the language decoder component. Accordingly, we decompose the $\text{VLM} = \text{LE} \circ \text{VE}$ into a fixed vision expert (VE) and a learnable language expert (LE) (*i.e.*, LLM decoder) denoted as function g_θ . For simplicity and clarity in this method, the multi-image fusion and projection layers are implicitly included within VE. We first define SFT on single image then show the SFT on inputs with reference images.

Single Query Image SFT. For ground-truth answer string, $a^* = \langle t_1, \dots, t_L \rangle$, the single image SFT on (X, Q, A) using generative VLM can be optimized via

$$\mathcal{L}_{\text{SFT}}(\theta) = - \sum_x \sum_j \log p_\theta(t_j | x, t_{<j}), \text{ where } p_\theta(t_j | x, t_{<j}) = \frac{\exp(g_\theta(x, t_{<j})_{t_j})}{\sum_{t' \in \mathcal{V}} \exp(g_\theta(x, t_{<j})_{t'})}, \quad (4)$$

where x is the input of LE as defined in Eq. 1.

Comparative SFT with Reference Images (SiP). We construct comparative SFT inputs as (X, X', Q, A) , wherein X -matched reference images X' are sampled using the strategy described in Sec. 3.1, specifically negative images that share diagnosis-irrelevant features. The SFT objective function is similar to Eq. 4, but with x replaced by Z' , where Z' is defined in Eq. 3. Furthermore, during training, multiple X' instances can be sampled for a given X to consist of various SFT tuples, and the model can be updated using the averaged gradient of these data.² Similarly, at inference time, multiple reference images can be sampled for the same query image, and the VLM can be prompted repeatedly. The resulting predictions can then be aggregated using ensemble strategies such as bagging to further enhance performance. Finally, we include example language prompts for both single-query inference and paired inference with a reference image in the Appendix.

4 Experiment

4.1 Settings

We first delineate our experimental settings below. Our code will be open-sourced upon acceptance.

Datasets and Modalities. In this study, we investigate the impact of incorporating reference images across several commonly used medical imaging modalities, including *chest X-rays*, *OCT RNFL thickness maps of the retina*, *dermatoscopic images*, and *color fundus*.

For the *chest X-ray* modality, the disease diagnosis task focuses on identifying two specific conditions—pneumonia and edema—which we refer to as CXP-Pneumonia and CXP-Edema, respectively. To facilitate this, we utilize two preprocessed test datasets provided by Jin et al.[23], both derived from the CheXpert dataset[24]. Each test set is class-balanced, comprising an equal number of

¹We set reference images as negative for 1. the ease of collection and 2. the flexibility to pair with different disease types.

²This is implemented by scaling the number of gradient accumulation steps in proportion to the number of reference images sampled per query. An ablation study illustrating this effect is provided in the Appendix.

positive and negative samples: 200 per class for *pneumonia* and 400 per class for *edema*. For *OCT RNFL thickness*, we utilize the GF3300 dataset [25], which includes both 2D and 3D imaging data of the retinal nerve fiber layer. We refer to this dataset as GF-Glaucoma. The testing set corresponds to the one preprocessed by FairMedFM [26], comprising 303 positive and 291 negative samples. For *dermatoscopy*, we use data from the HAM10000 dataset [27], a diverse collection of dermatoscopic images representing common pigmented skin lesions. We denote this dataset as HAM-Melanoma, with the testing set containing 212 melanoma and 189 benign keratosis-like lesion images. Finally, the color fundus dataset is sourced from the BRSET dataset [28], a publicly available collection of ophthalmological images from Brazilian patients, intended to support the development and evaluation of machine learning models for eye disease detection. We refer to it as BRSET-Retinopathy. The testing set includes 121 positive and 121 negative samples. The same testing datasets are consistently used for both off-the-shelf exploration in Sec. 3, and for the SFT evaluations presented below. The training datasets are sampled from the full datasets mentioned above, comprising a balanced set of 500 positive and 500 negative images, along with a reference pool. All training data strictly excludes any images used in testing. Further details on the composition of the training datasets used for SFT are provided in the Appendix.

Models. As mentioned in the Sec. 1, we focus on VLMs that both exhibit strong comparative reasoning capabilities and provide open-source fine-tuning code to facilitate lightweight adaptation. For assessing comparison capabilities, we refer to the benchmark proposed by Zhao et al. [11], which offers a comprehensive evaluation of existing VLMs on general-domain comparative tasks. We require selected models to support multi-image inference and, ideally, to incorporate medical domain priors for improved off-the-shelf performance. Among the benchmark results, Phi-3-4B and NVILA-7B demonstrate strong multi-image reasoning capabilities [9], which we decided to include into our study. Also, we include the recently released Qwen-2.5-VL-7B [8] as it exhibits good generalization performance and is also adapted in various medical VLM studies this year [29].

Evaluation Metrics. we employ the *Balanced Accuracy (BAcc.)* [30] and the *F1 score* [31] as our primary evaluation metrics. *BAcc.* computes the average of recall obtained on each class, thereby accounting for the imbalanced distribution by giving equal weight to each class regardless of their frequency. This metric ensures that performance on the minority class is not overshadowed by the majority class. Additionally, we use the *F1 score*, which is the harmonic mean of precision and recall, to evaluate the model’s ability to balance false positives and false negatives. The *F1 score* is particularly useful in imbalanced scenarios where high precision or recall alone may not be sufficient to reflect meaningful performance. Together, these metrics provide a more robust and fair assessment of classification effectiveness under skewed class distributions.

4.2 Exploration for SiP in Off-the-shelf Settings

Table 1: **Off-the-shelf diagnostic performance of VLMs across five medical imaging datasets, using either a single query image (“Single”) or a paired input with both query and reference images—denoted as SiP.** Three off-the-shelf VLMs are evaluated. For each dataset and model, the **best** result is highlighted in **yellow**. Across all settings, SiP consistently outperforms the single-image baseline, demonstrating the effectiveness of reference pairing in guiding diagnostic process. However, these off-the-shelf VLMs still exhibit limited medical prior in the current three general-purpose VLMs.

Model / Data	CXP-Pneumonia		CXP-Edema		GF-Glaucoma		HAM-Melanoma		BRSET-Retinopathy	
	Single	SiP	Single	SiP	Single	SiP	Single	SiP	Single	SiP
QwenVL-2.5-7B	57.50	59.50	49.88	52.62	52.39	52.58	52.56	54.52	52.48	57.44
NVILA-7B	71.75	73.25	71.12	81.13	49.99	55.63	48.09	50.00	50.83	61.57
Phi-3.5-4B	49.50	53.00	49.50	51.00	51.44	51.59	52.34	53.26	50.00	61.98

We begin by exploring how incorporating reference images affects the off-the-shelf diagnostic performance of VLMs. Specifically, we compare two prompting strategies: using a single image versus a paired input consisting of both the query and reference images, referred to as the SiP setting. The example data and prompt templates are provided in the Appendix. When evaluating the off-the-shelf performance, we randomly sampled three reference images for one query image and report

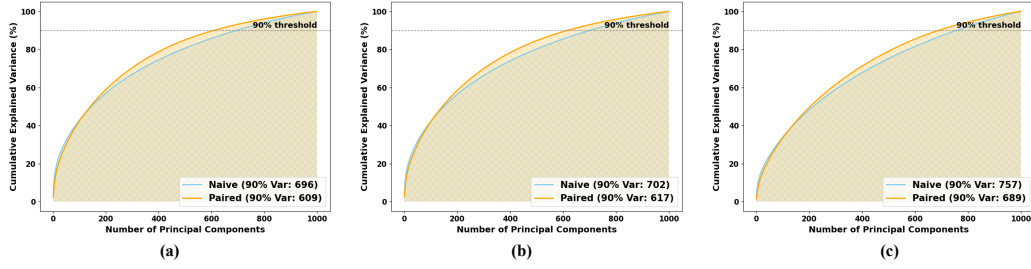


Figure 2: **PCA explained variance ratio comparison between naive and paired features across different modalities, where (a) shows the CXP-Pneumonia, (b) shows the CXP-Edema, and (c) shows the HAM-Melanoma.** The value of “90% Var” indicates the number of principal components required to reach 90% cumulative explained variance. The results show that paired features form a more compact, low-rank structure than naive ones: they require fewer components to reach 90% variance and concentrate more variance in the top principal components.

the mean performance as well as standard deviation in Appendix. While Table 1 summarizes the bagged performance (majority vote using the three runs) of three representative VLMs across five medical imaging datasets. As shown, in all cases, the SiP setting consistently outperforms the single-image setting, with best scores highlighted in yellow. This trend holds across different diseases and models, demonstrating the preliminary benefit of introducing reference-based comparative reasoning in medical image interpretation. However, we also note that the absolute AUC scores, even under the SiP setting, mostly range between 50%–60%, close to random chance. This observation indicates that while paired images introduce meaningful structure, the models still lack strong inherent medical priors necessary for confident diagnosis.

To further understand why paired inputs may benefit inference, we conducted a representational analysis based on PCA of visual encoder outputs. For each dataset, we extract image embeddings for NVILA-8B under both the single-image (naive) and SiP (paired) settings, and compute the cumulative explained variance across principal components. As shown in Figure 2, the SiP features exhibit a consistently more compact structure. We annotate the number of components needed to capture 90% of the total variance (denoted as “90% Var”) out of the original around 4K dimensional embedding inputs. For instance, in the CXP-Edema dataset, only 457 components are needed in the SiP setting, compared to 702 in the single-image setting—a 35% reduction. Similar trends are observed for CXP-Pneumonia and HAM-Melanoma. The cumulative variance curves clearly show that SiP features concentrate information in fewer dimensions, suggesting stronger feature alignment and reduced redundancy. This low-rank structure reflects more discriminative representations, which may explain the consistent performance gains observed with paired inputs. These findings offer a representation-level explanation for the benefits of reference-based VLM diagnosis, even in the absence of explicit medical supervision. Our further theoretical analysis in Sec 5 further consolidates the insights into improving representation generation by incorporating appropriate reference images in classification and diagnosis tasks.

4.3 Comparison to Baselines in SFT Settings

In this section, we begin to examine the effectiveness of incorporating the reference image within the SFT setting. Following the approach outlined in Sec. 3.2, we conduct the SFT study as described below.

Baselines. As described in Sec. 3, our main baseline is the single-image training group, in which we randomly sample 500 balanced positive and negative query images per modality from the original data pool (excluding the test set discussed earlier) to form the training set. The distribution of this data pool for each modality is provided in the Appendix. We refer to this straightforward baseline as “Single (w/o ref)” in Table 2. To reduce the effect of randomness in the sampling process, we repeat the data sampling three times and report the average performance for fairness. For SiP, reference images are randomly selected for the same set of query images from the same data pool. During inference, the model is given both the test query image and a randomly sampled reference image. Because

reference images can be drawn randomly, we can perform multiple inference passes per query and aggregate the results using majority voting (also known as bagging). The “SiP (w/ bagging)” setting denotes the scenario in which three inference passes—each using a different reference image—are conducted, and the final prediction is determined via majority voting.

Beyond this naive baseline, to provide a comprehensive performance comparison, we also include other settings. One straightforward setting is “Single (w/ ref)”, where our training data includes the 1000 query images above as well as all potential reference (healthy control) images in the data pool. However, this pool will be strongly unbalanced (with negative images dominate the data) as explained in the introduction and shown in the Appendix. We thus implemented several data-centric baseline methods that are commonly employed to address class imbalance issues in machine learning. These baselines serve as reference points for illustrating the effectiveness of SiP even under state-of-the-art sampling strategies.

Spatial Distribution-based Undersampling (SDUS) [32] is the on strategy that selectively removes the majority class instances based on their spatial distribution in the feature space, thereby preserving the decision boundaries and structural information. Another approach is Fuzzy C-means (FCM) clustering [33], which performs data reduction by grouping samples into clusters and selecting representative instances based on membership degrees, allowing for more nuanced undersampling than traditional methods. We also include the Undersampling based on Class instance density per Feature value intervals (UCF) method [34], which evaluates instance densities within specified feature intervals to identify and remove redundant majority class samples, thus retaining more discriminative data points. Finally, we consider bagging [35], an ensemble-based technique that aggregates the results from the FCM, SDUS, and UCF to enhance generalization and robustness. By incorporating both the naive single-image inference setting (“Single (w/o ref)”) and various data sampling strategies, our goal is to establish a rigorous framework for evaluating the effectiveness of reference data-based SFT performance and its approach to utilizing existing images.

Implementations. For all baseline groups, we use the Hugging Face Trainer ³ along with the Accelerate package ⁴ to perform distributed training of the VLMs across four A100 GPUs. Training is conducted with a per-device batch size of 1 and a learning rate of 1×10^{-4} . To ensure a fair comparison across all settings, we maintain a consistent number of training iterations (125 in this study) by adjusting the number of gradient accumulation steps according to the dataset sizes. More details is introduced in the Appendix.

Result Analysis. Table 2 presents the diagnostic performance of various methods across five medical imaging tasks spanning multiple data modalities. Across all datasets and model configurations, our method, SiP, consistently demonstrates superior performance—particularly in the SiP (pair-based inference) and SiP (w/ bagging) (ensemble of reference-inference results via majority voting) settings.

Firstly, SiP outperforms most baselines as shown by the highlighted colors in the bottom two rows, including both naive and advanced data-centric sampling strategies such as FCM, SDUS, UCF, and Bagging. Notably, in 10 out of 15 total AUC/F1 pairs, SiP or SiP (w/ bagging) achieves the best performance. The SiP (w/ bagging) setting sometimes yields the highest average AUC and F1 (especially on NVILA-8B), confirming the benefit of aggregating multiple reference-based inference passes.

The Single (w/o ref) and Single (w/ ref) settings perform poorly, particularly on complex datasets like HAM-Melanoma and GF-Glaucoma, highlighting the drawbacks of using randomly sampled single image for training and the drawbacks of the unbalanced reference pools when training with all data in the pool for Single (w/ ref). While UCF sometimes outperforms other baseline sampling strategies, it still lags behind SiP in both consistency and overall performance in most cases. Model-wise, all three VLMs benefit from reference-guided inference, with Qwen-VL-2.5-7B and NVILA-8B showing strong improvements and Qwen-VL-2.5-7B achieving the highest overall scores, demonstrating that SiP scales well with various models.

In summary, the results empirically validate the effectiveness of reference-guided inference using SiP and majority-voting-based aggregation. Unlike traditional data-centric baselines that rely on

³https://huggingface.co/docs/transformers/en/main_classes/trainer

⁴https://huggingface.co/docs/accelerate/package_reference/accelerator

Table 2: **Performance comparison across different data modalities for three VLM backbones on SFT: Qwen-VL-2.5-7B, Phi-3-4B, and NVILA-8B.** The table reports BAcc. and F1 scores for five medical datasets among the five columns. Each model is evaluated under various settings (baselines). The highlight of yellow and blue indicates the best and second best performance, respectively. The results show that incorporating SiP consistently improves performance. Thus, SiP provides a simple and effective strategy to improve VLM performance.

Settings	CXP-Pneumonia		CXP-Edema		GF-Glaucoma		HAM-Melanoma		BERST-Retinopathy	
	BAcc.	F1	BAcc.	F1	BAcc.	F1	BAcc.	F1	BAcc.	F1
Qwen-VL-2.5-7B										
Single (w/o ref)	64.42	56.39	68.87	66.07	64.29	67.88	68.68	60.81	71.07	63.00
Single (w/ ref)	50.00	0.00	50.00	0.00	50.00	0.00	55.99	25.00	50.00	0.00
Single (w/ ref) + FCM [33]	58.50	33.60	68.63	72.92	56.90	26.48	65.05	53.50	68.60	59.14
Single (w/ ref) + SUDS [32]	66.25	54.85	67.75	61.49	64.37	60.19	68.33	63.40	71.90	65.66
Single (w/ ref) + UCF [34]	67.25	63.91	70.13	74.27	62.55	61.08	62.13	48.70	72.31	72.65
Single (w/ ref) + Bagging	65.50	53.06	69.62	72.97	63.97	63.36	64.09	55.28	71.90	66.00
SiP	70.75	68.12	74.88	76.16	67.34	71.30	76.17	73.94	76.86	76.66
SiP (w/ bagging)	70.25	67.40	75.25	76.54	66.41	70.80	75.46	72.92	76.03	75.63
Phi-3-4B										
Single (w/o ref)	61.83	46.01	62.45	47.74	61.61	47.52	64.47	52.94	72.45	70.18
Single (w/ ref)	50.00	0.00	50.00	0.00	57.32	32.11	42.09	59.57	50.00	0.00
Single (w/ ref) + FCM [33]	53.75	14.75	65.62	56.69	59.71	42.00	62.87	49.84	73.55	72.17
Single (w/ ref) + SUDS [32]	59.00	34.40	55.00	23.40	65.58	56.42	60.33	39.71	69.42	63.73
Single (w/ ref) + UCF [34]	64.50	52.35	72.12	74.04	65.37	57.38	62.51	47.49	68.18	72.00
Single (w/ ref) + Bagging	59.00	33.87	65.75	56.23	65.09	55.32	62.04	46.46	73.55	72.17
SiP	66.25	60.41	69.50	64.84	64.08	68.36	71.80	64.46	74.38	69.61
SiP (w/ bagging)	66.00	59.76	69.75	64.62	67.29	71.06	71.45	64.90	75.62	71.50
NVILA-8B										
Single (w/o ref)	78.50	79.42	83.45	84.49	65.32	65.56	70.24	69.41	74.24	76.91
Single (w/ ref)	50.25	1.00	51.62	6.75	58.99	35.08	43.93	63.12	50.83	4.80
Single (w/ ref) + FCM [33]	76.00	78.57	84.00	85.39	63.29	63.91	71.51	72.99	73.55	78.23
Single (w/ ref) + SUDS [32]	78.25	77.99	83.37	84.97	62.85	62.22	71.37	69.13	75.45	77.49
Single (w/ ref) + UCF [34]	70.75	76.36	76.25	80.53	49.89	66.82	70.38	69.70	74.79	77.14
Single (w/ ref) + Bagging	76.00	78.51	83.12	84.78	62.42	63.62	71.15	70.38	75.52	78.05
SiP	79.25	78.44	84.88	85.51	69.61	65.83	75.17	74.30	76.45	77.65
SiP (w/ bagging)	79.50	78.65	85.00	85.51	69.13	64.49	74.65	73.92	77.27	78.26

class balancing during training, SiP fully leverages healthy control images and incorporates these contextual signals at inference time. This approach offers a simple yet highly effective strategy to enhance VLM performance in realistic, negative-dominated medical imaging scenarios.

5 Theory

In this section, we provide theoretical evidence for why SiP works. For simplicity, instead of next token prediction, we study the task of binary classification.⁵ We will show that pairing examples with “reference examples” can lead to faster statistical convergence properties compared to the naive strategy of adding these reference examples as additional rows in the training set.

Formally, consider a joint distribution $P = P_{X,Y}$ on $\mathcal{X} \times \{\pm 1\}$, where \mathcal{X} is the input space and the label space is binary. Let P_{-1} and P_1 denote the conditional distributions on \mathcal{X} given $Y = -1$ and $Y = 1$ respectively. The input distribution is then equal to the mixture $P_X := \pi_{-1}P_{-1} + \pi_1P_1$, where $\pi_{-1} = \mathbb{P}_P(Y = -1)$, $\pi_1 = \mathbb{P}_P(Y = 1)$.

To formalize the nature of a reference example, we define a joint distribution \tilde{P} on $\mathcal{X} \times \mathcal{X}$, such that

$$\int_{\mathcal{X}} \tilde{P}(\cdot, dx) = P_X, \quad \int_{\mathcal{X}} \tilde{P}(dx, \cdot) = P_{-1}.$$

For every draw $(X, X') \sim \tilde{P}$, we call X' the reference (example) of X . We can think of it as a fresh negative example that was chosen to be similar to X , with the similarity being defined via \tilde{P} .⁶ Assume that we have IID training examples $\mathcal{D}_n := \{(X_i, X'_i, Y_i)\}_{i=1}^n$, with $(X_i, X'_i) \sim \tilde{P}$

⁵This simplification approach was also taken previous work studying properties of transformers [36, 37]. We focus on the closed-form QA binary diagnosis first and then scale to autoregressive generation later.

⁶In probability theory, such a joint distribution is called a *coupling* between P_X and P_{-1} .

and $Y_i \sim P_{Y|X_i}$. The goal is to train a classifier \hat{c} to predict the label Y of a new example X , having observed $(X, X') \sim \tilde{P}$. The performance of such a classifier will be measured in terms of its misclassification error: $R(\hat{c}) = \mathbb{P}_{(X, X') \sim \tilde{P}, Y \sim P_{Y|X}}[\hat{c}(X, X') \neq Y]$.

We now formalize the two training strategies we wish to compare. Consider two feature embeddings: $\phi_{\text{naive}}: \mathcal{X} \rightarrow \mathbb{R}^d$ and $\phi_{\text{paired}}: \mathcal{X} \times \mathcal{X} \rightarrow \mathbb{R}^d$. These can be thought of as modeling the image encoder applied to single images and paired images respectively. We will make use of two further simplifications: (1) We assume that ϕ_{naive} and ϕ_{paired} are fixed and do not depend on data. (2) We constrain our hypothesis classes to be linear in either of these representations and optimize over them via the support vector machine (SVM) algorithm. Specifically, we define the *paired* classifier as $\hat{c}_{\text{paired}}(x, x') = \text{sign}(\hat{w}^\top \phi_{\text{paired}}(x, x') + b)$, where

$$\hat{w}, \hat{b} = \arg \max \left\{ \min_{1 \leq i \leq n} Y_i (w^\top \phi_{\text{paired}}(X_i, X'_i) + b) : \|w\|_2 = 1, |b| \leq M_{\text{paired}} \right\}, \quad (5)$$

where $M_{\text{paired}} = (\mathbb{E}_{\tilde{P}} \|\phi_{\text{paired}}(X, X')\|_2^2)^{1/2}$. We define the *naive* classifier as $\hat{c}_{\text{naive}}(x, x') = \text{sign}(\hat{w}^\top \phi_{\text{naive}}(x) + b)$, where the parameters are optimized after adding the reference examples as additional training examples. In other words, we set $X_{n+i} = X'_i$, $Y_{n+i} = -1$ for $i = 1, 2, \dots, n$, and take

$$\hat{w}, \hat{b} = \arg \max \left\{ \min_{1 \leq i \leq 2n} Y_i (w^\top \phi_{\text{naive}}(X_i) + b) : \|w\|_2 = 1, |b| \leq M_{\text{naive}} \right\}, \quad (6)$$

where $M_{\text{naive}} = (\mathbb{E}_P \|\phi_{\text{naive}}(X)\|_2^2)^{1/2}$. Note that we have assumed for simplicity that the classification problem is separable under both representations. The maximum value in (5) is called the margin of \hat{c}_{paired} and is denoted as ρ_{paired} . Similarly, define ρ_{naive} .

Theorem 1. *For any $\delta > 0$, with probability at least $1 - \delta$, we have*

$$R(\hat{c}_{\text{paired}}) \leq \frac{8M_{\text{paired}}/\rho_{\text{paired}}}{\sqrt{n}} + \sqrt{\frac{\log \log_2(2M_{\text{paired}}/\rho_{\text{paired}})}{n}} + \sqrt{\frac{\log(2/\delta)}{2n}}, \quad (7)$$

$$R(\hat{c}_{\text{naive}}) \leq \frac{8M_{\text{naive}}/\rho_{\text{naive}}}{\sqrt{n}} + \sqrt{\frac{\log \log_2(2M_{\text{naive}}/\rho_{\text{naive}})}{n}} + \sqrt{\frac{\log(2/\delta)}{n}}. \quad (8)$$

This theorem, which follows from somewhat standard results, is proved in Appendix. In each of these two bounds, the first term is the main term and is derived from Rademacher complexity [38], which is commonly used to characterize the statistical hardness of learning problems. As such, if the ratios satisfy $M_{\text{paired}}/\rho_{\text{paired}} \ll M_{\text{naive}}/\rho_{\text{naive}}$, we see that *the paired classifier is more statistically efficient than the naive classifier, despite both algorithms seeing the same amount of information.*

To give some further intuition, suppose that we can decompose the naive feature embedding into unknown “relevant” and “nuisance” components: $\phi_{\text{naive}}(x) = (\psi_{\text{rel}}(x), \psi_{\text{nu}}(x))$. We assume further that: (1) The class Y is independent of $\psi_{\text{nu}}(X)$; (2) Each example shares the same nuisance component as its reference: $\psi_{\text{nu}}(X) = \psi_{\text{nu}}(X')$. Hence, having a reference example helps us to isolate the relevant part of X as the subvector in which it differs from its reference. Defining the paired representation to be $\phi_{\text{paired}}(x, x') := \phi_{\text{naive}}(x) - \phi_{\text{naive}}(x') = (\psi_{\text{rel}}(x) - \psi_{\text{rel}}(x'), 0)$, we see that the upper bound M_{paired} can be significantly reduced from M_{naive} if the nuisance component has high energy. In summary, the pairing strategy allows us to automatically perform sufficient dimension reduction [39]. Although, in a linear setting, dimension reduction can be performed using feature selection techniques, such strategies may not be available when we work with complicated architectures such as VLMs.

6 Conclusion

This work underscores the value of reference image-guided comparative reasoning in enhancing medical image diagnosis using VLMs. Drawing direct inspiration from clinical practices, we show that incorporating healthy control reference images—paired with structured prompts—enables general-purpose VLMs to outperform traditional single-image baselines across a variety of imaging modalities. Our proposed “See-in-Pairs” (SiP) framework offers a lightweight yet effective SFT strategy that

not only boosts diagnostic accuracy but also improves feature compactness and sample efficiency. Theoretical analysis further supports our findings, demonstrating improved statistical convergence when using paired representations. Altogether, our study provides compelling empirical and theoretical evidence for embracing comparative inference in future medical AI systems, advocating for a paradigm shift toward more clinically-aligned and interpretable VLM architectures.

Acknowledgments and Disclosure of Funding

We gratefully acknowledge the support from the Natural Sciences and Engineering Research Council of Canada (NSERC), the Canadian Institutes of Health Research (CIHR), the Canada Foundation for Innovation (CFI), the Mitacs program, the CIFAR AI Chair Award, the Canada Research Chair Fellowship, Canada NSERC, the IITP grant funded by the Ministry of Science and ICT, Korea, the Gemini Academic Program, the UBC Advanced Research Computing, and Digital Research Alliance of Canada.

References

- [1] Dinggang Shen, Guorong Wu, and Heung-Il Suk. Deep learning in medical image analysis. *Annual review of biomedical engineering*, 19(1):221–248, 2017.
- [2] Syed Muhammad Anwar, Muhammad Majid, Adnan Qayyum, Muhammad Awais, Majdi Alnowami, and Muhammad Khurram Khan. Medical image analysis using convolutional neural networks: a review. *Journal of medical systems*, 42:1–13, 2018.
- [3] Muhammad Imran Razzak, Saeeda Naz, and Ahmad Zaib. Deep learning for medical image processing: Overview, challenges and the future. *Classification in BioApps: Automation of decision making*, pages 323–350, 2017.
- [4] Heang-Ping Chan, Ravi K Samala, Lubomir M Hadjiiski, and Chuan Zhou. Deep learning in medical image analysis. *Deep learning in medical image analysis: challenges and applications*, pages 3–21, 2020.
- [5] Zhihong Chen, Yan Song, Tsung-Hui Chang, and Xiang Wan. Generating radiology reports via memory-driven transformer. *arXiv preprint arXiv:2010.16056*, 2020.
- [6] Chunyuan Li, Cliff Wong, Sheng Zhang, Naoto Usuyama, Haotian Liu, Jianwei Yang, Tristan Naumann, Hoifung Poon, and Jianfeng Gao. Llava-med: Training a large language-and-vision assistant for biomedicine in one day. *Advances in Neural Information Processing Systems*, 36:28541–28564, 2023.
- [7] Omkar Thawkar, Abdelrahman Shaker, Sahal Shaji Mullappilly, Hisham Cholakkal, Rao Muhammad Anwer, Salman Khan, Jorma Laaksonen, and Fahad Shahbaz Khan. Xraygpt: Chest radiographs summarization using medical vision-language models. *arXiv preprint arXiv:2306.07971*, 2023.
- [8] Shuai Bai, Keqin Chen, Xuejing Liu, Jialin Wang, Wenbin Ge, Sibong Song, Kai Dang, Peng Wang, Shijie Wang, Jun Tang, et al. Qwen2. 5-vl technical report. *arXiv preprint arXiv:2502.13923*, 2025.
- [9] Zhijian Liu, Ligeng Zhu, Baifeng Shi, Zhuoyang Zhang, Yuming Lou, Shang Yang, Haocheng Xi, Shiyi Cao, Yuxian Gu, Dacheng Li, et al. Nvila: Efficient frontier visual language models. *arXiv preprint arXiv:2412.04468*, 2024.
- [10] Marah Abidin, Jyoti Aneja, Hany Awadalla, Ahmed Awadallah, Ammar Ahmad Awan, Nguyen Bach, Amit Bahree, Arash Bakhtiari, Jianmin Bao, Harkirat Behl, et al. Phi-3 technical report: A highly capable language model locally on your phone. *arXiv preprint arXiv:2404.14219*, 2024.
- [11] Bingchen Zhao, Yongshuo Zong, Letian Zhang, and Timothy Hospedales. Benchmarking multi-image understanding in vision and language models: Perception, knowledge, reasoning, and multi-hop reasoning. *arXiv preprint arXiv:2406.12742*, 2024.
- [12] Muntasir Wahed, Kiet A Nguyen, Adheesh Sunil Juvekar, Xinzhuo Li, Xiaona Zhou, Vedant Shah, Tianjiao Yu, Pinar Yanardag, and Ismini Lourentzou. Prima: Multi-image vision-language models for reasoning segmentation. *arXiv preprint arXiv:2412.15209*, 2024.
- [13] Nima Tajbakhsh, Jae Y Shin, Suryakanth R Gurudu, R Todd Hurst, Christopher B Kendall, Michael B Gotway, and Jianming Liang. Convolutional neural networks for medical image analysis: Full training or fine tuning? *IEEE transactions on medical imaging*, 35(5):1299–1312, 2016.
- [14] Tri Huynh, Aiden Nibali, and Zhen He. Semi-supervised learning for medical image classification using imbalanced training data. *Computer methods and programs in biomedicine*, 216:106628, 2022.
- [15] Wisdom Ikezogwo, Saygin Seyfioglu, Fatemeh Ghezloo, Dylan Geva, Fatwir Sheikh Mohammed, Pavan Kumar Anand, Ranjay Krishna, and Linda Shapiro. Quilt-1m: One million image-text pairs for histopathology. *Advances in neural information processing systems*, 36:37995–38017, 2023.

- [16] Yukun Zhou, Mark A Chia, Siegfried K Wagner, Murat S Ayhan, Dominic J Williamson, Robbert R Struyven, Timing Liu, Moucheng Xu, Mateo G Lozano, Peter Woodward-Court, et al. A foundation model for generalizable disease detection from retinal images. *Nature*, 622(7981):156–163, 2023.
- [17] Kai Zhang, Rong Zhou, Eashan Adhikarla, Zhiling Yan, Yixin Liu, Jun Yu, Zhengliang Liu, Xun Chen, Brian D Davison, Hui Ren, et al. A generalist vision–language foundation model for diverse biomedical tasks. *Nature Medicine*, pages 1–13, 2024.
- [18] Jong Hak Moon, Hyungyung Lee, Woncheol Shin, Young-Hak Kim, and Edward Choi. Multi-modal understanding and generation for medical images and text via vision-language pre-training. *IEEE Journal of Biomedical and Health Informatics*, 26(12):6070–6080, 2022.
- [19] Yunyi Liu, Zhanyu Wang, Dong Xu, and Luping Zhou. Q2atransformer: Improving medical vqa via an answer querying decoder. In *International conference on information processing in medical imaging*, pages 445–456. Springer, 2023.
- [20] Josh Achiam, Steven Adler, Sandhini Agarwal, Lama Ahmad, Ilge Akkaya, Florencia Leoni Aleman, Diogo Almeida, Janko Altschmidt, Sam Altman, Shyamal Anadkat, et al. Gpt-4 technical report. *arXiv preprint arXiv:2303.08774*, 2023.
- [21] Haotian Liu, Chunyuan Li, Yuheng Li, Bo Li, Yuanhan Zhang, Sheng Shen, and Yong Jae Lee. Llava-next: Improved reasoning, ocr, and world knowledge, January 2024.
- [22] Quan Sun, Yufeng Cui, Xiaosong Zhang, Fan Zhang, Qiying Yu, Yuezhe Wang, Yongming Rao, Jingjing Liu, Tiejun Huang, and Xinlong Wang. Generative multimodal models are in-context learners. In *Proceedings of the IEEE/CVF Conference on Computer Vision and Pattern Recognition*, pages 14398–14409, 2024.
- [23] Ruinan Jin, Wenlong Deng, Minghui Chen, and Xiaoxiao Li. Debaised noise editing on foundation models for fair medical image classification. In *International Conference on Medical Image Computing and Computer-Assisted Intervention*, pages 164–174. Springer, 2024.
- [24] Jeremy Irvin, Pranav Rajpurkar, Michael Ko, Yifan Yu, Silviana Ciurea-Ilcus, Chris Chute, Henrik Marklund, Behzad Haghighi, Robyn Ball, Katie Shpanskaya, et al. Chexpert: A large chest radiograph dataset with uncertainty labels and expert comparison. In *Proceedings of the AAAI conference on artificial intelligence*, volume 33, pages 590–597, 2019.
- [25] Yan Luo, Yu Tian, Min Shi, Louis R Pasquale, Lucy Q Shen, Nazlee Zebardast, Tobias Elze, and Mengyu Wang. Harvard glaucoma fairness: a retinal nerve disease dataset for fairness learning and fair identity normalization. *IEEE Transactions on Medical Imaging*, 2024.
- [26] Ruinan Jin, Zikang Xu, Yuan Zhong, Qingsong Yao, DOU QI, S Kevin Zhou, and Xiaoxiao Li. Fairmedfm: fairness benchmarking for medical imaging foundation models. *Advances in Neural Information Processing Systems*, 37:111318–111357, 2024.
- [27] Philipp Tschandl, Cliff Rosendahl, and Harald Kittler. The ham10000 dataset, a large collection of multi-source dermatoscopic images of common pigmented skin lesions. *Scientific data*, 5(1):1–9, 2018.
- [28] Luis Filipe Nakayama, David Restrepo, João Matos, Lucas Zago Ribeiro, Fernando Korn Malerbi, Leo Anthony Celi, and Caio Saito Regatieri. Brset: a brazilian multilabel ophthalmological dataset of retina fundus photos. *PLOS Digital Health*, 3(7):e0000454, 2024.
- [29] Yuxiang Lai, Jike Zhong, Ming Li, Shitian Zhao, and Xiaofeng Yang. Med-r1: Reinforcement learning for generalizable medical reasoning in vision-language models. *arXiv preprint arXiv:2503.13939*, 2025.
- [30] Kay Henning Brodersen, Cheng Soon Ong, Klaas Enno Stephan, and Joachim M Buhmann. The balanced accuracy and its posterior distribution. In *2010 20th international conference on pattern recognition*, pages 3121–3124. IEEE, 2010.
- [31] David MW Powers. Evaluation: from precision, recall and f-measure to roc, informedness, markedness and correlation. *arXiv preprint arXiv:2010.16061*, 2020.

- [32] Yuanting Yan, Yuanwei Zhu, Ruiqing Liu, Yiwen Zhang, Yanping Zhang, and Ling Zhang. Spatial distribution-based imbalanced undersampling. *IEEE Transactions on Knowledge and Data Engineering*, 35(6):6376–6391, 2022.
- [33] Vibha Pratap and Amit Prakash Singh. Novel fuzzy clustering-based undersampling framework for class imbalance problem. *International Journal of System Assurance Engineering and Management*, 14(3):967–976, 2023.
- [34] Fei Wang, Ming Zheng, Kai Ma, and Xiaowen Hu. Resampling approach for imbalanced data classification based on class instance density per feature value intervals. *Information Sciences*, 692:121570, 2025.
- [35] Leo Breiman. Bagging predictors. *Machine learning*, 24:123–140, 1996.
- [36] Shivam Garg, Dimitris Tsipras, Percy Liang, and Gregory Valiant. What can transformers learn in-context? a case study of simple function classes. In Alice H. Oh, Alekh Agarwal, Danielle Belgrave, and Kyunghyun Cho, editors, *Advances in Neural Information Processing Systems*, 2022.
- [37] Emmanuel Abbe, Samy Bengio, Aryo Lotfi, Colin Sandon, and Omid Saremi. How far can transformers reason? the globality barrier and inductive scratchpad. In *The Thirty-eighth Annual Conference on Neural Information Processing Systems*, 2024.
- [38] M. Mohri, A. Rostamizadeh, and A. Talwalkar. *Foundations of Machine Learning, second edition*. Adaptive Computation and Machine Learning series. MIT Press, 2018.
- [39] Kofi P Adragani and R Dennis Cook. Sufficient dimension reduction and prediction in regression. *Philosophical Transactions of the Royal Society A: Mathematical, Physical and Engineering Sciences*, 367(1906):4385–4405, 2009.
- [40] Jiazhen Pan, Che Liu, Junde Wu, Fenglin Liu, Jiayuan Zhu, Hongwei Bran Li, Chen Chen, Cheng Ouyang, and Daniel Rueckert. Medvbm-r1: Incentivizing medical reasoning capability of vision-language models (vlms) via reinforcement learning. *arXiv preprint arXiv:2502.19634*, 2025.
- [41] Pengfei Li, Gang Liu, Jinlong He, Zixu Zhao, and Shenjun Zhong. Masked vision and language pre-training with unimodal and multimodal contrastive losses for medical visual question answering. In *International Conference on Medical Image Computing and Computer-Assisted Intervention*, pages 374–383. Springer, 2023.
- [42] Yeongjae Cho, Taehee Kim, Heejun Shin, Sungzoon Cho, and Dongmyung Shin. Pretraining vision-language model for difference visual question answering in longitudinal chest x-rays. *arXiv preprint arXiv:2402.08966*, 2024.
- [43] Zhihong Shao, Peiyi Wang, Qihao Zhu, Runxin Xu, Junxiao Song, Xiao Bi, Haowei Zhang, Mingchuan Zhang, YK Li, Y Wu, et al. Deepseekmath: Pushing the limits of mathematical reasoning in open language models. *arXiv preprint arXiv:2402.03300*, 2024.
- [44] Michael Moor, Qian Huang, Shirley Wu, Michihiro Yasunaga, Yash Dalmia, Jure Leskovec, Cyril Zakka, Eduardo Pontes Reis, and Pranav Rajpurkar. Med-flamingo: a multimodal medical few-shot learner. In *Machine Learning for Health (ML4H)*, pages 353–367. PMLR, 2023.
- [45] Junying Chen, Chi Gui, Ruyi Ouyang, Anningzhe Gao, Shunian Chen, Guiming Hardy Chen, Xidong Wang, Ruifei Zhang, Zhenyang Cai, Ke Ji, et al. Huatuogpt-vision, towards injecting medical visual knowledge into multimodal llms at scale. *arXiv preprint arXiv:2406.19280*, 2024.
- [46] Luis-Jesus Marhuenda, Miquel Obrador-Reina, Mohamed Aas-Alas, Alberto Albiol, and Roberto Paredes. Unveiling differences: A vision encoder-decoder model for difference medical visual question answering. In *Medical Imaging with Deep Learning*.
- [47] Alistair EW Johnson, Tom J Pollard, Seth J Berkowitz, Nathaniel R Greenbaum, Matthew P Lungren, Chih-ying Deng, Roger G Mark, and Steven Horng. Mimic-cxr, a de-identified publicly available database of chest radiographs with free-text reports. *Scientific data*, 6(1):317, 2019.

- [48] Vardan Papyan, XY Han, and David L Donoho. Prevalence of neural collapse during the terminal phase of deep learning training. *Proceedings of the National Academy of Sciences*, 117(40):24652–24663, 2020.
- [49] Sadhika Malladi, Alexander Wettig, Dingli Yu, Danqi Chen, and Sanjeev Arora. A kernel-based view of language model fine-tuning. In *International Conference on Machine Learning*, pages 23610–23641. PMLR, 2023.

Contents

1	Introduction	1
2	Related Work	2
3	See-in-Pairs (SiP) VLMs with Reference images	3
3.1	SiP Inference	3
3.2	Improved Performance via Comparative Supervised Fine-tuning (SFT)	4
4	Experiment	4
4.1	Settings	4
4.2	Exploration for SiP in Off-the-shelf Settings	5
4.3	Comparison to Baselines in SFT Settings	6
5	Theory	8
6	Conclusion	9
A	Notations	16
B	Related Work	16
C	Data Distribution	17
D	Implementation details	18
D.1	Baselines	18
D.2	Visualization of Data	19
E	Additional Results	20
E.1	Off-the-shelf performance on Medical VLMs	20
E.2	Empirical Validation of the Theorem 1	21
E.3	Ablation Study on the Scale of Reference Images	22
E.4	Computational Cost	22
E.5	Influence of the Center for Reference Image Sampling	23
F	Proof of Theorem 1	23

A Notations

Table 3: Summary of notation used throughout the paper.

Symbol	Description
\mathcal{X}	Space of medical images $\mathbf{X} \in \mathcal{X}$
\mathcal{Q}	Space of natural-language prompts $Q \in \mathcal{Q}$
\mathcal{A}	Candidate answer set $A = \{a_1, \dots, a_K\}$
a_k, t_i, L_k	k -th answer string, its i -th token and length
Z	Serialized single-image embedding $\langle \text{encoder}(X), \text{encode}(Q) \rangle$
X'	Matched <i>reference</i> (negative) image
Z'	Paired embedding $\langle \text{fusion}(\text{enc}(X), \text{enc}(X')), \text{enc}(Q) \rangle$
θ	All trainable parameters of the VLM
VE, LE	Frozen Vision expert / learnable Language expert
g_θ	Language-decoder function after decomposition $\text{VLM} = \text{LE} \circ \text{VE}$
$\mathcal{L}_{\text{SFT}}(\theta)$	Supervised-fine-tuning loss (Eq. 4)
$t_{<j}, \mathcal{V}$	Previous tokens and vocabulary in next-token loss
$P_{X,Y}$	Joint distribution on inputs and binary labels $Y \in \{\pm 1\}$
P_{-1}, P_1	Class-conditional distributions $P_{X Y=-1}, P_{X Y=1}$
π_{-1}, π_1	Class priors $P(Y = -1), P(Y = 1)$
\hat{P}	Coupling on (X, X') used to sample references
D_n	Training set $\{(X_i, X'_i, Y_i)\}_{i=1}^n$
$\varphi_{\text{naive}}, \varphi_{\text{paired}}$	Single- vs. paired-image feature maps
$\hat{c}_{\text{naive}}, \hat{c}_{\text{paired}}$	Corresponding linear SVM classifiers
w, b	Weight vector and bias of a linear classifier
$M_{\text{naive}}, M_{\text{paired}}$	Radius (norm bound) of each feature space
$\rho_{\text{naive}}, \rho_{\text{paired}}$	Geometric margin achieved by each SVM
$R(\hat{c})$	Mis-classification error of a classifier
n	Number of training triples (X, X', Y)
σ_i	Rademacher variables in complexity analysis
$\Phi_\rho(\cdot)$	Ramp loss with parameter ρ
$H_{\text{naive}}, H_{\text{paired}}$	Hypothesis classes for the two representations

B Related Work

Image Comparison in General Vision-Language Models Recent general-purpose VLMs have increasingly incorporated capabilities for image comparison by leveraging architectural advances and multimodal training strategies. Qwen-VL-2.5-Instruct [8] enables fine-grained visual comparison through co-attention-based multimodal fusion, image-specific positional encoding, and instruction tuning on comparative reasoning tasks. NVILA-8B [9] employs a “scale-then-compress” architecture that allows high-resolution and long-context visual input, supporting nuanced relational reasoning across images. Phi-3.5-Vision [10] introduces interleaved visual-text token processing, facilitating multi-hop relational inference across multiple images in a single context window. While these models demonstrate impressive general-purpose comparative reasoning, they are trained on generic visual data and lack domain-specific priors crucial for specialized applications such as medicine. This limits their ability to perform clinically meaningful comparisons, such as disease progression analysis or inter-patient comparisons involving nuanced pathologies.

Image Comparison in Medical Vision-Language Models In the medical domain, the bulk of recent VLMs have been developed for single-image or single-series (e.g., longitudinal studies from one patient) understanding [5, 6, 7, 40, 41, 42], with comparatively little emphasis on cross-image

comparison. Table 4 summarizes how eleven such models align with three perspectives: cross-image comparative priors, medical-domain pretraining, and open-weight availability.

Generalist architectures QwenVL-2.5-Instruct [8] and Phi-3.5-Vision [10] benefit from large-scale, multi-image pretraining and are released with open weights, yet they lack any medical-domain supervision. In contrast, R2Gen [5], XrayGPT [7], and MUMC [41] incorporate radiology-specific pretraining on individual images; LLaVaMed [6] is an instruction-tuned adaptation of a generalist VLM trained on a large single-image medical corpus; MedVLM-R1 [40] leverages reinforcement learning with GRPO [43] using single-image inputs; and Plural [42] specializes in longitudinal-series analysis of a given patient’s study. All of these remain confined to single-image or series-based workflows without native cross-image comparison.

Emerging multi-image medical VLMs such as MedFlamingo⁷ [44], NVILA [9], and HuatuoGPT-Vision⁸ [45] demonstrate the feasibility of integrating medical priors with comparative reasoning. However, they are not extensively trained for various medical modalities nor diverse multi-image comparison datasets. Despite these early efforts to mimic clinical workflows requiring paired-view or longitudinal reasoning, truly general-purpose, open-weight medical VLMs capable of robust cross-image comparison remain scarce. This underscores the need for unified comparative training objectives that generalize across modalities, view-pairs, and pathologies without bespoke, task-specific engineering.

Table 4: **Properties of the existing VLMs.**

Model	Cross-image Comparative Prior	Medical Prior	Open-Weights
QwenVL-2.5-Instruct [8]	✓	✗	✓
Phi-3.5-Vision [8]	✓	✗	✓
R2Gen [5]	✗	✓	✓
LLaVaMed [6]	✗	✓	✓
XrayGPT [7]	✗	✓	✓
MedVLM-R1 [40]	✗	✓	✓
MUMC [41]	✗	✓	✓
Plural [42]	✗	✓	✓
VEDVQA [46]	✗	✓	✗
MedFlamingo [44]	✓	✓	✗
NVILA [9]	✓	✓	✓
HuatuoGPT-Vision [45]	✓	✓	✓

C Data Distribution

Table 5a shows the distribution of our *data pool* and Table 5b shows the distribution of our *testing pool*. In the data pool (Table 5a), each dataset includes a fixed number of 500 positive samples, but the number of negative samples varies significantly to mimic the practical scenario that healthy control dominates the medical dataset, ranging from 900 in HAM-Melanoma to over 13,000 in CXP-Pneumonia. This leads to different class distribution across datasets to make our experimental setting comprehensive. On the other hand, the testing set (Table 5b) has a more balanced distribution between positive and negative samples within each dataset, supporting fairer evaluation across classes.

As will introduced in App. D.1 in more detail, during training, we explore how easily available healthy control images can be leveraged by comparing seven configurations (Table 2), all using the same 500 positives per modality and the full pool of healthy negatives (Table 5a), but differing in which negatives are actually seen. The *Single (w/o ref)* baseline trains on only the 500 positive and 500 randomly sampled negative *query* images per modality, yielding a perfectly balanced 1 000-image set and no auxiliary references at either stage. To test whether gains stem merely from seeing more healthy images, *Single (w/ ref)* keeps the same balanced query set but also feeds every remaining negative image during training—and one random reference at test—while three undersampling

⁷The checkpoint was inaccessible during preparation of this paper as shown [here](#).

⁸We have not evaluated this VLM extensively due to its limited performance on diagnostic and comparative tasks (App. E.1).

strategies (FCM, SUDS, UCF) curb the resulting imbalance. Our method, SiP, retains the identical 500 + 500 queries yet couples each query with a randomly drawn healthy control to create explicit query–reference *pairs*, training the VLM to focus on relational differences rather than absolute appearance⁹. At inference a single (or three, with bagging) fresh reference is sampled from the pool, harnessing the full reservoir of negatives without skewing class balance. Together, these settings disentangle the effects of data volume, class balance and pairwise reasoning on diagnostic performance.

Table 5: **Class distribution in *data pool* and *testing splits*.** (a) illustrates the class distribution within the data pool, where training data is sampled from them, as introduced later. Our training dataset consistently includes 500 positive examples. Negative examples are either fully or partially sampled, depending on the baseline being evaluated. Reference images are drawn from the same pool. (b) presents the distribution of the testing data, which is strictly separated from the *data pool*. The CXR-Edema and CXR-Pneumonia datasets were collected by Jin et al.[23], while GF-Glaucoma, HAM-Melanoma, and BRSET-Retinopathy are sourced from FairMedFM[26] as described in Sec. 4.

Category	Positive	Negative	Category	Positive	Negative
CXP-Edema	500	12 853	CXP-Edema	400	400
CXP-Pneumonia	500	13 292	CXP-Pneumonia	200	200
GF-Glaucoma	500	1 261	GF-Glaucoma	303	291
HAM-Melanoma	500	900	HAM-Melanoma	212	189
BRSET-Retinopathy	500	8 352	BRSET-Retinopathy	121	121

(a)

(b)

D Implementation details

This section provides the detailed implementation for the experimental results in the Sec. 4 of the main paper. The code will be open-sourced upon acceptance.

Off-the-shelf inference. For off-the-shelf inference, we run each VLM on a single A100 GPU and prompt it using the base prompt shown in Fig. 3, concatenated with a chain-of-thought prompt (e.g., “Think step by step and provide your final answer at the end.”)¹⁰. For all models and datasets, we will launch the model for three times and report the average and standard deviation, where the results is shown in table and table. Additionally, we will ensemble the three runs using majority voting, where the results is shown in table and table.

SFT. For all three VLMs, we use the Hugging Face Trainer with the `accelerate` launch command and DeepSpeed ZeRO-2 mode, running on four NVIDIA GPUs. To enable efficient fine-tuning, we incorporate LoRA with rank of 16. For all of our baselines except the single (w/ref), we control the number of updates (iterations) to be the 125 regardless of the number of data points in the training set. This is achieved by scaling the number of gradient accumulation steps by the same scale of the dataset sizes¹¹.

D.1 Baselines

Our primary aim is to show how easily available healthy control images can be leveraged alongside query images. To this end, we compare seven configurations (Table 2), all drawing from the same

⁹This study focuses on the 1,000 query images used for training, as our goal—outlined in Sec. 1—is to *efficiently* adapt general-purpose VLMs for medical comparison with strong generalizability, especially given the high cost of acquiring positive samples in practice.

¹⁰We found that the chain-of-thought prompt significantly improves model performance compared to directly prompting the VLM for an answer, which often causes the VLM to default to “yes” or “no” based on its language priors.

¹¹Note that the modern accelerator package and similar packages will scale the loss by the scale of the gradient accumulation steps and the distributed parallel parameters as shown [here](#).

pool of positives (500 per modality) and negatives (all remaining healthy images, see Table 5a), but differing in which negatives they actually see.

Single (w/o ref). This vanilla baseline uses exactly 500 positive and 500 negative *query* images per modality for training, with no auxiliary reference images at train or test time. These images are randomly sampled from the data pool and for fairness, we sampled three subsets to train three models, and report the average testing result.

Single (w/ ref). To rule out the possibility that our paired approach simply benefits from extra negatives, we give the model the same 500 positives and 500 negatives as queries *plus all* remaining negative images as references during training. At test time a single random reference is also supplied. This exposes the model to the full healthy pool but creates a heavily imbalanced training set. As the training set is imbalanced and the VLM may feel challenge to learn them, we plug in three strategies to mitigate the strongly imbalanced data, *FCM* [33], *SUDS* [32], *UCF* [34]. *FCM* [33] clusters the healthy references with fuzzy C-means and keeps the samples whose membership to their centroid is highest, ensuring that only prototypical, low-variance negatives remain. *SUDS* [32] constructs sphere-neighborhood graphs in the embedding space and selects a spatially uniform subset that preserves the global geometry of the majority class, thereby avoiding the local redundancy associated with random undersampling. Finally, *UCF* [34] partitions each feature dimension into equal-width intervals, estimates class-instance density within every interval, and preferentially retains negatives from sparse regions while discarding those in over-populated bins, yielding a set with near-uniform class frequency across the feature space.

Bagging. To further enhance robustness and reduce variance, we form an ensemble by combining the three baselines (*FCM*, *SUDS* and *UCF*) into a single prediction. At test time, each of the three models produces an independent prediction for a given query images; these predictions are then fused via majority voting to yield the final class label. This aggregation scheme leverages the complementary strengths of the individual baseline criteria—prototypicality, spatial coverage and density uniformity—so that errors made by any single method can be outvoted by the others. Empirically, bagging in this way has been shown to stabilize decision boundaries and improve generalization under distributional shift [35].

SiP. We construct 1000 balanced *paired* samples per modality by matching each query image (500 positive and 500 negative, as in the *Single (w/o ref)* setting) with a randomly sampled negative reference from the *data pool*, ensuring that the healthy control images are fully utilized. During training, the VLM learns to distinguish positive from negative queries in the context of a specific reference, encouraging the model to capture relational cues between query–reference pairs. At inference time, each query is evaluated alongside a single, randomly selected negative reference from the data pool. To mitigate variability introduced by the stochastic reference selection, we perform inference three times using different random seeds—thus varying the reference set—and report the average results over these three independent runs.

SiP (w/ bagging). The training procedure is identical to that of SiP, using 500 positive and 500 negative query–reference pairs per modality. At test time, however, we sample three distinct negative references for each query and generate three independent predictions. Instead of averaging performance scores, we aggregate the three predictions via majority voting to determine the final class label. This strategy harnesses complementary evidence from multiple references and helps reduce the influence of any single reference’s variability on the model’s final decision.

Reference Image Sampling. To the extent possible, reference images are selected to match key demographic attributes. Specifically, for CXP-Edema and CXP-Pneumonia, we match on patient gender, image view (frontal vs. lateral), and acquisition type (AP vs. PA); for GF-Glaucoma and BRSET, we match on gender; and for HAM-Melanoma, we match on anatomical location (from the *localization* column). If no image satisfies all criteria—due to limited sample availability—we select the closest matching reference or fall back to random sampling from the remaining pool.

D.2 Visualization of Data

Figure 3 illustrates representative query images and root prompts for both single (*w/o reference*) and paired (*w/ reference*) configurations across the four tasks in our study.

Table 6: Overview of baseline configurations and their defining traits.

Baseline	Key characteristic
Single (w/o ref)	500 positives + 500 negatives as queries; no references at train or test.
Single (w/ ref)	Same queries supplemented with <i>all</i> remaining healthy controls as inputs during training.
Single (w/ ref) + FCM	Selects 500 representative negatives from the full reference pool via fuzzy C-means clustering to preserve prototypical samples.
Single (w/ ref) + SUDS	Chooses 500 negatives by spatially uniform sampling in the embedding space to maintain global coverage.
Single (w/ ref) + UCF	Samples 500 negatives based on feature-interval density to ensure uniform representation across feature dimensions.
Single (w/ ref) + Bagging	Aggregates the three baseline models (FCM, SUDS, UCF) by majority voting at test time.
SiP	Trains on 500 balanced paired queries (positive/negative) each matched with a unique reference; uses a single random reference per query at test.
SiP (w/ bagging)	Same training as SiP; at test, draws three random references per query and fuses their outputs via majority vote.

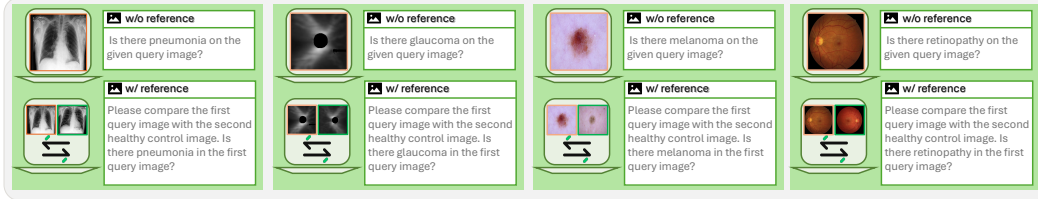


Figure 3: **Example query images and root prompts.** Shown for the single (*w/o reference*) and paired (*w/ reference*) settings across four modalities: chest X-rays for pneumonia, fundus images for glaucoma, dermoscopic images for melanoma, and retinal scans for retinopathy. In the single setting (top row), the model sees only the query image and is asked a direct diagnostic question. In the paired setting (bottom row), the model receives both a query and a healthy reference image and is prompted to compare them.

E Additional Results

E.1 Off-the-shelf performance on Medical VLMs

Table 7: **Off-the-shelf performance (AUC, %) of three VLMs across five diagnostic datasets.** Results are shown for both the single (*w/o reference*) and comparative (*w/ reference*) settings. Performance is reported as mean \pm standard deviation over three independent runs.

Model / Data	CXP-Pneumonia		CXP-Edema		GF-Glaucoma		HAM-Melanoma		BERST-Retinopathy	
	Single	Comparative	Single	Comparative	Single	Comparative	Single	Comparative	Single	Comparative
QwenVL-2.5-7B-Instruct	56.75 \pm 0.86	58.58\pm1.76	49.92 \pm 0.07	52.29\pm0.81	51.58 \pm 0.84	52.23\pm0.58	52.46 \pm 1.64	55.00\pm0.83	53.03 \pm 0.63	53.72\pm0.83
NVILA-7B	71.66\pm0.14	70.33 \pm 0.63	71.04 \pm 0.38	76.45\pm1.31	49.99 \pm 0.00	54.40\pm1.46	47.76 \pm 0.13	49.64\pm0.49	50.83 \pm 0.00	58.26\pm3.60
Phi-3.5-4B	50.66 \pm 0.95	53.33\pm2.98	49.38 \pm 0.00	50.13\pm0.99	51.44 \pm 0.00	52.50\pm0.74	52.76 \pm 0.14	53.48\pm0.60	50.14 \pm 0.24	60.47\pm1.04

Table 7 presents the off-the-shelf performance of QwenVL-2.5-7B-Instruct, NVILA-7B and Phi-3.5-4B on CXP-Pneumonia, CXP-Edema, GF-Glaucoma, HAM-Melanoma and BERST-Retinopathy under both single and comparative prompting. Introducing a negative reference at test time yields consistent improvements for most model-task pairs: QwenVL gains between +1.83 and +2.54 points, NVILA-7B increases by +1.88 to +7.43 points (with a slight -1.33 drop on pneumonia as exception), and Phi-3.5-4B improves by +0.72 to +10.33 points, the largest boost occurring on retinopathy. These results highlight the efficacy of comparative prompting—especially for modalities with subtle visual differences—while the minor performance decrease for NVILA-7B on pneumonia suggests that reference-based comparisons may interact in nuanced ways with specific model architectures.

Table 8: **Off-the-shelf performance of medical VLMs on the five imaging diagnostic benchmarks.** For each dataset, we report zero-shot AUC (%) in two evaluation settings: *Single*, where the model selects an answer independently, and *Comparative*, where it must decide which of two alternatives better matches the image. HuatuoVision-7B and LLaVaMed-7B are evaluated with and without test-time bagging. Mean \pm standard deviation is computed over three random seeds. Across all datasets, accuracies remain close to random-guess level ($\sim 50\%$), and no method shows reliable gains in the more challenging comparative setting, highlighting the limited cross-modal and comparison ability of current medical VLMs.

Model / Data	CXP-Pneumonia		CXP-Edema		GF-Glaucoma		HAM-Melanoma		BERST-Retinopathy	
	Single	Comparative	Single	Comparative	Single	Comparative	Single	Comparative	Single	Comparative
HuatuoVision-7B	51.25 \pm 0.66	53.17 \pm 3.02	50.71 \pm 0.29	54.96 \pm 0.40	49.63 \pm 1.03	49.62 \pm 0.69	50.49 \pm 1.25	51.03 \pm 2.75	51.79 \pm 0.95	50.69 \pm 4.01
HuatuoVision-7B (w/ bagging)	50.25	55.75	50.12	55.75	50.56	50.93	50.24	49.86	50.00	49.17
LLaVaMed-7B	49.25 \pm 1.73	49.00 \pm 1.75	49.96 \pm 1.73	48.00 \pm 1.47	49.76 \pm 1.27	48.20 \pm 1.28	50.54 \pm 0.71	47.27 \pm 0.67	51.24 \pm 1.43	51.65 \pm 2.89
LLaVaMed-7B (w/ bagging)	51.00	50.25	50.12	47.63	49.16	47.05	50.80	47.73	50.00	56.20

Table 8 reveals that current off-the-shelf *medical VLMs* struggle to perform reliably on image-based medical diagnostic tasks under the same settings, *especially in the image comparison settings*. Across all five datasets and both evaluation metrics, model performance hover around the random baseline of 50%, indicating minimal learned understanding of the underlying visual pathology. Notably, performance in the *comparative* setting, which demands higher-level reasoning to choose the better-matching answer from two alternatives, does not improve and often declines relative to the *single* setting. This suggests that current medical VLMs lack effective cross-image reasoning capabilities (also validated by their single image dominant training-set as introduced in Sec. 2) and are particularly weak in tasks requiring comparative judgment. Overall, these results emphasize the need for more specialized training strategies that go beyond generic VLM pre-training to equip models with domain-specific visual understanding and comparison skills. This observation also motivates our decision to center the main paper on three open-source VLMs that natively support comparative prompting, allowing us to systematically assess how reference-based inference influences performance across different model architectures.

E.2 Empirical Validation of the Theorem 1

In this subsection, we delve deeper into the empirical validation of our theorem.

Experimental Set-up. The evaluation covers the five medical-imaging datasets used in the main paper (CXP-Pneumonia, CXP-Edema, GF-Glaucoma, HAM-Melanoma and BRSET-Retinopathy), each randomly subsampled to $n = 1,000$ image-reference pairs. Images are embedded once with the frozen NVILA-7B, yielding a (256,3584)-dimensional hidden size for each image. For the naïve baseline, we vectorise the embedding, $\phi_{\text{naive}}(X) = \text{vec}(E(X))$; for the proposed method we subtract the reference image before vectorising to maintain the dimension to be the same, $\phi_{\text{paired}}(X, X') = \text{vec}(E(X) - E(X'))$. The complexity term is approximated by $M = \sqrt{\max_i \sum_j (\phi_{ij} - \bar{\phi}_i)^2}$, while the geometric margin $\rho = 2/\|w\|_2$ is extracted from a linear SVM trained on the same representation. Computing the ratio M/ρ for both feature maps yields a direct proxy for the excess-risk bound in Theorem 1.

Table 9: **Empirical validation of Theorem 1.** For five medical-imaging benchmarks, we report the empirical counterpart of the statistical-hardness factor M/ρ that appears in Eqs. (7)–(8). *Single* uses the naïve, single-image representation ϕ_{naive} ; $M_{\text{paired}}/\rho_{\text{paired}}$ is the same quantity computed on the paired representation $\phi_{\text{paired}}(x, x')$. Smaller values imply an easier learning problem. Across all tasks the paired representation yields a markedly smaller factor, supporting the prediction that the paired classifier enjoys tighter excess-risk bounds and therefore faster convergence.

Model / Data	CXP-Pneumonia		CXP-Edema		GF-Glaucoma		HAM-Melanoma		BRSET-Retinopathy	
	$M_{\text{naive}}/\rho_{\text{naive}}$	$M_{\text{paired}}/\rho_{\text{paired}}$	$M_{\text{naive}}/\rho_{\text{naive}}$	$M_{\text{paired}}/\rho_{\text{paired}}$	$M_{\text{naive}}/\rho_{\text{naive}}$	$M_{\text{paired}}/\rho_{\text{paired}}$	$M_{\text{naive}}/\rho_{\text{naive}}$	$M_{\text{paired}}/\rho_{\text{paired}}$	$M_{\text{naive}}/\rho_{\text{naive}}$	$M_{\text{paired}}/\rho_{\text{paired}}$
NVILA-7B	34.33	26.50	24.94	19.43	33.80	26.06	27.52	22.11	59.38	41.77

Result analysis. Table 9 shows the results for empirical validation of Theorem 1. On every dataset the paired representation lowers the hardness factor: M/ρ drops from 34.3 to 26.5 on CXP-Pneumonia, from 24.94 to 19.43 on CXP-Edema, from 33.80 to 26.06 on GF-Glaucoma, from

27.52 to 22.11 on HAM-Melanoma, and from 59.38 to 41.77 on BRSET-Retinopathy. These reductions of roughly 20–30% mirror the inequality $M_{\text{paired}}/\rho_{\text{paired}} < M_{\text{naive}}/\rho_{\text{naive}}$, so the paired classifier is more statistically efficient than the naive classifier.

E.3 Ablation Study on the Scale of Reference Images

In this part, we analyze the effect of the number of reference images.

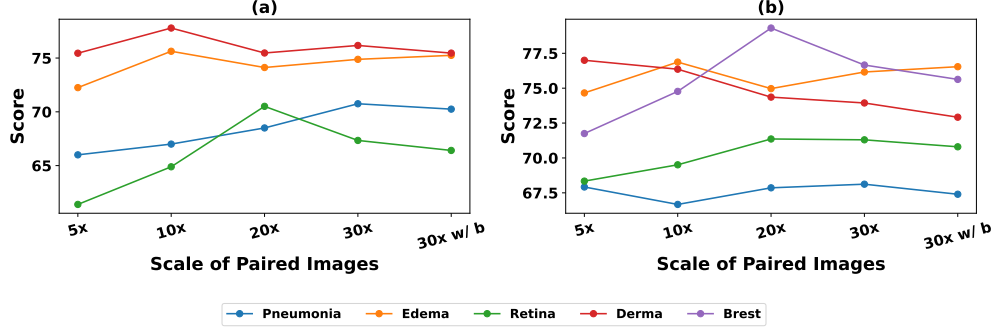


Figure 4: **Impact of the number of reference images.** Each curve corresponds to one of the five benchmarks. The x -axis gives the ratio K of reference images to every query image ($5\times, 10\times, 20\times, 30\times$); the right-most tick ($30\times$ w/b) still trains with $K = 30$ but, at test time, samples three references and aggregates their predictions by majority vote. The left subfig. (a) presents the BAcc. and the right subfig. (b) presents F1.

Result analysis. Fig. 4 shows the result for ablating the number of reference images. As shown, for every dataset performance rises steadily from $5\times$ to $30\times$, indicating that additional references increase the probability of selecting a truly informative counterpart and thereby increase the effective margin of the paired representation. Beyond this point gains saturate and in several cases (*e.g.*, Pneumonia-BAcc. and Derma-F1) drift downward, suggesting that very large reference pools introduce redundant or noisy comparisons that outweigh the benefit of extra signal. The bagged variant ($30\times$ w/b) mitigates this effect: by sampling only three references per test image and voting, it suppresses outliers while still exploiting the richer pool, recovering or surpassing the peak scores achieved at $20\times$. Overall, the curve shapes confirm a regime of diminishing returns in which a moderate number of diverse reference images—around $30\times$ in our setting—strikes the best balance between additional information and noise-induced variance.

E.4 Computational Cost

Table 10 presents the computational cost per inference, measured in FLOPs, for three models—Qwen-2.5-VL-7B, Phi-3.5-4B, and NVILA-7B—under two settings: *Single* (using only the single image) and *SiP* (using the single image along with reference images). This evaluation is conducted using the SFT model on the pneumonia dataset.

From the results, we observe that incorporating reference images in the SiP setting consistently increases the computational cost across all models. Specifically, Qwen-2.5-VL-7B sees an increase from 3.47×10^{12} to 6.63×10^{12} FLOPs, nearly doubling the computation. Phi-3.5-4B shows a similar trend, with FLOPs rising from 7.99×10^{12} to 16.31×10^{12} . Interestingly, NVILA-7B, despite having the highest cost in the Single setting (4.27×10^{13}), shows only a modest increase in the SiP setting (8.99×10^{12}), which is lower than both Qwen-2.5-VL-7B and Phi-3.5-4B under SiP. This indicates that NVILA-7B may be more efficient at leveraging reference images compared to the other models, because it employs a different “scale-then-compress” architecture.

Table 10: **Computational cost per inference measured by FLOPs.**

Settings / Models	Qwen-2.5-VL-7B	Phi-3.5-4B	NVILA-7B
Single	3.47×10^{12}	7.99×10^{12}	42.70×10^{12}
SiP	6.63×10^{12}	1.63×10^{13}	8.99×10^{12}

E.5 Influence of the Center for Reference Image Sampling

In the previous baseline results, reference images were sampled from the data pool collected at a single medical center. In this subsection, we examine a more realistic scenario where reference images are drawn from a held-out dataset originating from a different medical center. Specifically, we sample reference images from MIMIC-CXR [47] while evaluating query images on CheXpert [24].

Setup. To assess the robustness of the model to the choice of reference image source, we evaluate performance when reference images are sampled from either the same dataset as the query set (CheXpert) or a different dataset (MIMIC-CXR). We use the Qwen-VL-2.5-7B model and report performance on two clinical benchmarks: CXP-Pneumonia and CXP-Edema. For each task, we evaluate using BAcc. and F1 score.

Analysis. As shown in Table 11, the model performs comparably regardless of whether the reference images are sourced from CheXpert or MIMIC-CXR. For CXP-Pneumonia, the performance remains stable (BAcc: 70.75 vs. 69.75; F1: 68.12 vs. 68.07). Similarly, for CXP-Edema, performance is consistent or slightly improved when using references from MIMIC-CXR (BAcc: 74.88 vs. 75.12; F1: 76.16 vs. 76.56). These results suggest that reference images sampled from an external medical center can still provide effective guidance, demonstrating the model’s capacity to generalize across different clinical data sources.

Table 11: **Comparison of performance when reference images are sourced from different medical centers.** Query images are from CheXpert [24], while reference images are sampled either from the same dataset (CheXpert) or a different dataset (MIMIC-CXR [47]). Results show that reference images from an external center (MIMIC-CXR) yield comparable performance, indicating strong cross-center generalization.

Settings	CXP-Pneumonia		CXP-Edema	
	BAcc.	F1	BAcc.	F1
Qwen-VL-2.5-7B				
SiP (CheXpert)	70.75	68.12	74.88	76.16
SiP (MIMIC-CXR)	69.75	68.07	75.12	76.56

F Proof of Theorem 1

The proof follows an immediate consequence of Theorem 5.9 in [38], but with some modifications.

First, given a dataset $S = \{Z_1, Z_2, \dots, Z_m\}$, with $Z_i \in \mathbb{R}^d$ for $i = 1, 2, \dots, m$, and a hypothesis class H comprising functions $h: \mathbb{R}^d \rightarrow \mathbb{R}$, recall that the empirical Rademacher complexity of H with respect to S is given by

$$\widehat{\mathfrak{R}}_S(H) := \frac{1}{m} \mathbb{E}_\sigma \left[\sup_{h \in H} \sum_{i=1}^m \sigma_i h(Z_i) \right],$$

where $\sigma = (\sigma_1, \sigma_2, \dots, \sigma_m)$ is a vector of IID Rademacher random variables. If $Z_1, Z_2, \dots, Z_M \sim_{IID} D$ for some distribution D , the Rademacher complexity of H is defined as

$$\mathfrak{R}_{m,D}(H) := \mathbb{E}_{S \sim_{IID} D} [\widehat{\mathfrak{R}}_S(H)].$$

Lemma 2. *Let*

$$H_{\text{paired}} = \{w^\top \phi_{\text{paired}}(x, x') + b : \|w\|_2 = 1, |b| \leq M_{\text{paired}}\},$$

$$H_{\text{naive}} = \{w^\top \phi_{\text{naive}}(x) + b : \|w\|_2 = 1, |b| \leq M_{\text{naive}}\}.$$

We have

$$\mathfrak{R}_{n, \tilde{P}}(H_{\text{paired}}) \leq \frac{2M_{\text{paired}}}{\sqrt{n}} \quad (9)$$

$$\mathfrak{R}_{n, P}(H_{\text{naive}}) \leq \frac{2M_{\text{naive}}}{\sqrt{n}} \quad (10)$$

Proof. Let Φ denote the $n \times p$ matrix whose i -th row is given by $\phi_{\text{paired}}(X_i, X'_i)$. We have

$$\begin{aligned} \hat{\mathfrak{R}}_{\mathcal{D}_n}(H_{\text{paired}}) &= \frac{1}{n} \mathbb{E}_\sigma \left[\sup_{\|w\|_2 \leq 1} \sigma^\top \Phi w + \sup_{|b| \leq M_{\text{paired}}} b \sum_{i=1}^n \sigma_i \right] \\ &= \frac{1}{n} \mathbb{E}_\sigma \left[\|\sigma^\top \Phi\|_2 + M_{\text{paired}} \left| \sum_{i=1}^n \sigma_i \right| \right] \\ &\leq \frac{M_{\text{paired}}}{n} \mathbb{E}_\sigma \left[\|\sigma^\top \Phi\|_2^2 \right]^{1/2} + \frac{1}{n} \mathbb{E}_\sigma \left[\left| \sum_{i=1}^n \sigma_i \right|^2 \right]^{1/2} \\ &= \frac{1}{n} \text{Trace}(\Phi^\top \Phi)^{1/2} + \frac{M_{\text{paired}}}{\sqrt{n}} \\ &= \frac{1}{\sqrt{n}} \left(\left(\frac{1}{n} \sum_{i=1}^n \|\phi_{\text{paired}}(X_i, X'_i)\|_2^2 \right)^{1/2} + M_{\text{paired}} \right). \end{aligned}$$

Taking expectations and using Cauchy-Schwarz completes the proof of (9). Proving (10) is completely analogous. \square

To prove (7), we now simply apply Theorem 5.9 in [38], use H_{paired} for the hypothesis class, and select $\rho = \rho_{\text{paired}}$.

Proving (8) is slightly more complicated because of the non-IID nature of \mathcal{D}'_{2n} . To address this, for any $\rho > 0$, define the function

$$\Phi_\rho(x) = \begin{cases} 0 & \text{if } \rho \leq x, \\ 1 - x/\rho & \text{if } 0 \leq x \leq \rho, \\ 1 & \text{if } x \leq 0. \end{cases}$$

Note that the loss function $L_\rho(y, y') = \Phi_\rho(yy')$ dominates zero-one loss. For a hypothesis h , denote the empirical margin loss as

$$\hat{R}_{\rho, S}(h) = \frac{1}{m} \sum_{i=1}^m \Phi_\rho(y_i h(Z_i)).$$

Now, let $\mathcal{D}''_n = \{(X_i, Y_i)\}_{i=1}^n$. Using Theorem 5.9 in [38], we get an event with probability at least $1 - \delta$ on which

$$R(\hat{c}_{\text{naive}}) \leq \hat{R}_{\rho, \mathcal{D}''_n}(h) + \frac{4}{\rho} \mathfrak{R}_n(H_{\text{naive}}) + \sqrt{\frac{\log \log_2(2M_{\text{naive}}/\rho)}{n}} + \sqrt{\frac{\log(2/\delta)}{n}} \quad (11)$$

for any $0 < \rho < M_{\text{naive}}$. Finally, recognize that for any $h \in H_{\text{naive}}$, we have

$$\hat{R}_{\rho, \mathcal{D}''_n}(h) \leq \frac{1}{2} \hat{R}_{\rho, \mathcal{D}'_n}(h).$$

By definition \hat{c}_{naive} has a margin of ρ_{naive} , which implies that $\Phi_{\rho_{\text{naive}}}(Y_i(\hat{w}^\top \phi_{\text{naive}}(X_i) + \hat{b}_i)) \geq \rho_{\text{naive}}$ for $i = 1, 2, \dots, 2n$, so that $\hat{R}_{\rho_{\text{naive}}, \mathcal{D}'_n}(\hat{c}_{\text{naive}}) = 0$. It follows that $\hat{R}_{\rho, \mathcal{D}''_n}(\hat{c}_{\text{naive}}) = 0$. Plugging this back into (11) completes the proof of (8).

Remark 3 (Scope of the linear-head assumption). *Throughout Section 5 we analyse predictors of the form $h(x) = w^\top \phi(x) + b$ with a frozen encoder ϕ and a trainable linear head. Furthermore, we assume that the classes are linearly separable under the encoder representation. These assumptions help us to explain SiP by cleanly isolating one mechanism by which it can enhance the efficiency of SFT—by reducing the ratio M/ρ —thereby yielding higher accuracy (see Table 9). At the same time, we believe that our assumptions align with how SiP, and deep learning models more generally, work in practice. First, in the fine-tuning protocol adopted in Section 4, the vision backbone of the VLM remains fixed and only a lightweight classification layer (LoRA-enabled linear layers) is updated. Empirically, modern over-parameterised networks rapidly enter a regime where the penultimate embeddings are themselves linearly separable and optimization converges to the max-margin solution [48]; recent kernel-regime analyses of large language models further indicate that full fine-tuning often behaves like training a linear predictor in a fixed feature space [49]. Consequently, while end-to-end VLMs are nonlinear, the linear-head assumption is both faithful to the fine-tuning strategy evaluated in this work and sufficiently expressive to capture the margin geometry that governs generalisation in over-parameterised models.*

Broader Impact

This work proposes SiP, a clinically inspired method for enhancing VLMs in medical imaging diagnosis through the use of healthy reference images and comparative reasoning. By emulating the diagnostic practices of clinicians—who often compare patient scans to prior or normative examples—SiP improves model interpretability, alignment with human decision-making, and diagnostic accuracy, particularly in under-resourced settings. This approach enables general-purpose VLMs to perform more reliably on medical tasks via lightweight fine-tuning, reducing reliance on large-scale domain-specific datasets. However, it also raises considerations around bias in reference selection, the need for careful curation of reference pools, and the importance of retaining human oversight in clinical decision-making. More broadly, SiP offers a blueprint for incorporating structured, comparative inputs into multimodal models across domains requiring fine-grained visual distinction, suggesting new directions for interpretable and context-aware AI systems.

Limitations

While this paper explores clinically motivated comparative medical image analysis using vision-language models, its scope is limited to closed-ended, answer-only diagnosis tasks currently. Also, involving SiP will incur unavoidable inference time computing. However, such inference time computing will improve the performance of the model.